

Additively manufactured novel Al-Cu-Sc-Zr alloy: Microstructure and Mechanical properties

Priyanka Agrawal^{a,b}, Sanya Gupta^a, Saket Thapliyal^{a,b}, Shivakant Shukla^{a,b,1}, Ravi Sankar Haridas^{a,b}, Rajiv S. Mishra^{a,b}

^aCenter for Friction Stir Processing, Department of Materials Science and Engineering, University of North Texas, Denton, TX 76207 USA

^bAdvanced Materials and Manufacturing Processes Institute, University of North Texas, Denton, TX 76207, USA

*Corresponding author: Rajiv.Mishra@unt.edu

¹Current address: Oak Ridge National Laboratory, Oak Ridge, TN 37830, USA

Abstract

An in-depth understanding of microstructure and resultant properties is paramount in the design of a novel alloy system, especially for additive manufacturing (AM). The present investigation aims to characterize a prototypical AM Al alloy with great potential for structural applications. An Al-1.5Cu-0.8Sc-0.4Zr alloy designed using integrated computational material engineering was printed using the laser powder bed fusion AM process. This novel alloy shows promising combination of strength and ductility in as-built and peak-aged conditions. This improvement in the tensile properties is attributed to the presence of both coherent L1₂ Al₃Sc/Al₃(Sc,Zr) precipitates and Cu-rich regions. The microstructures were studied via extensive microscopy at different length scales using X-ray microscopy, scanning electron microscopy, and transmission electron microscopy. Fractography revealed that the columnar grain boundaries in as-built condition allow easy slip transfer as compared to the equiaxed grains, with the apex of the melt pool acting as the crack nucleation site. However, the peak aged condition resulted in improved strength while marginally sacrificing ductility due to precipitates decorating dislocations, grain boundaries and melt pool boundaries thus acting as obstacles to slip transfer.

Keywords: additive manufacturing; aluminum alloys; X-ray microscopy; texture; fractography

1. Introduction

Additive manufacturing (AM) is the state of the art technology where 3D components in metals are built by adding layer on layer of the powder material and fused using a laser or electron source. AM is gaining popularity as fabrication of intricately shaped components is possible without requiring long supply chain processes [1,2]. In recent years, AM of alloys such as Ti-6Al-4V [3,4], Al alloys [5–7], Nickel-based IN series [8,9], high-strength steels [10–12] and high-entropy alloys [13,14] have been studied extensively.

Laser powder bed fusion (LPBF) process is one such AM technique where the powder bed is selectively melted with the laser beam in an inert atmosphere [6]. The laser beam fuses the powder at specific locations defined by the computer aid design (CAD). After fusion of one layer, the next layer of powder is coated and the process is repeated till a 3D component with desired geometry is obtained.

LPBF gives higher degrees of freedom to tailor the properties of the final finished product by altering the printing (process) parameters such as laser power, powder particle size distribution, laser scan speed, hatch spacing, the angle between the consecutive layers (inter-layer rotation), and layer thickness [1,2,7,15–18]. These parameters need to be optimized to get a high-quality build with minimal amount of pores, and no cracks, as the tuning of the microstructure is only possible to a limited extent, due to process-specific characteristics such as the pore size and density, melt pool size, grain size, morphology and orientation, etc. Furthermore, LPBF process involves a high cooling rate of the order of 10^4 to 10^7 K/s [6] and hence can produce microstructures and properties different from the alloys produced through conventional routes. Despite these advantages, there are a limited number of structural materials available for printing with LPBF due majorly to printability related issues such as solidification cracking and process

induced pores.

Recently Thapliyal et al. [13,19] and Zhou et al. [20] reported via Scheil-Gulliver non-equilibrium solidification simulation that to obtain good printability, a small solidification range (T_L-T_s) along with less crack susceptibility is required [5,6,21]. A system with eutectic solidification at the terminal stage, as predicted by CALPHAD, potentially leads to minimal thermal contraction strains and thus is less susceptible to hot-cracking [15,17,19].

Aluminum and its alloys are widely used in structural applications due to its unique combination of properties such as high specific strength, and good corrosion resistance [22,23] making them popular next to steel. However, printing of Al alloys via LPBF is a challenge because of solidification cracking [6,7]. This limits the use of additively manufactured Al alloys in critical structural applications such as marine and aerospace. Among the Al alloys, AM of Al-Si alloys, which are eutectic-based, has been studied widely; these alloys are shown to have good printability [6,24–26].

The high strength Al alloys have shortcomings for printing due to solidification cracking, among which were 2XXX [27] and 7XXX [5,28,29]. This leads to the need to study and improve the printability of Al alloys. Koutny et al. [27] studied different scan strategies via LPBF of Cu containing 2618 Al alloy where solidification cracks were reported and the yield and tensile strength of the as-printed sample were half of values for the extruded material. Wang et al. [30] studied Al-3.5wt%Cu-1.5wt%Mg-1wt%Si to improve the printability and corrosion resistance with the addition of Si and Mg respectively. As-built samples tested exhibited ~225 MPa yield strength (YS) and ~365 MPa tensile strength whereas T6 aging treatment lead to 50% improvement in YS and 20% in tensile strength attributed to $\text{Al}_2\text{Cu}(\text{Mg})$ precipitates refining the microstructure.

Studies on the addition of Sc to the wrought Al and its alloys e.g. Al-Cu, Al-Mg-Si, Al-Zn-Mg and Al-Li by Røyset et al. [31] and Toropova et al. [32] showed improvement in mechanical properties due to formation of Al_3Sc precipitates. For additively manufacturing Al alloys, Schmidtke et al. [17] reported that the addition of Sc leads to improved printability and mechanical properties. From thermodynamic studies, Sc forms low-temperature eutectic at low wt.% in Al alloys [33,34]. Thus, the addition of Sc leads to crack-healing effect, as also reported by Qbau et al. [35], and therefore improves printability. Refined microstructure and improved mechanical properties with Sc addition were due to L1_2 Al_3Sc precipitates.

Chen et al. [36] compared Al-2.5Cu-0.3Sc (wt.%) with Sc-free alloy. The Sc solute atoms were observed to promote uniform precipitation of finer θ' Al_2Cu particles and thus significant increase in hardness (~90%). The mechanism was understood to be the solute-vacancy and solute-solute interactions where Sc is predominantly present as solute atoms for Al-Cu-Sc alloys. From Al-Sc alloys, Sc, if partially replaced by Zr, also leads to almost dense, and crack-free builds. Knipling et al. [33] reported that completely replacing Sc with Zr does not provide competing mechanical properties. But a partial replacement of Sc with Zr leads to $\text{Al}_3(\text{Sc},\text{Zr})$ precipitates, and this has been reported to improve the mechanical properties as compared to Al_3Sc ones. With Al-0.06Sc, a peak hardness of 429 MPa was achieved at 325°C, whereas for Al-0.06Zr, the peak hardness was 295 MPa at 475°C. With the presence of both Sc and Zr, above 325°C, a secondary peak hardness of 618 MPa was observed around 400°C due to Zr-rich precipitates.

To complement the good corrosion resistance of Al-Mg alloys with improved printability and mechanical properties, Sc and Zr have been added to these alloys. The reports and findings mainly resulted from an almost dense and crack-free builds with a bi-modal microstructures with

improved corrosion resistance. Li et al. [37] studied binary Al-6.2Mg alloy for the addition of Sc-Zr where improved corrosion resistance was reported. Spierings et al. [38,39] and Zhou et al. [40,41] studied Al-Mg-Zn-Sc-Zr alloy leading to similar findings where the melt pool regions close to the pool base showed $\text{Al}_3(\text{Sc},\text{Zr})$ and Al-Mg oxides leading to a refined microstructure. Other Sc- and Zr-containing alloys also include Al-Cu-Mg-Zr [42], Al-Cu-Mg-Mn-Zr [43], Al-Mg-Si-Cu-Sc-Zr [44], Al-Si-Mg-Sc-Zr [44,45] alloys where just Zr or synergistic effect of Sc and Zr were studied with other alloying elements. Poor printability of Al alloys prevents the use of additively manufactured Al alloys in structural application. This provides motivation to develop Al alloys with combination of improved properties and good printability.

For the current Al-Cu-Sc-Zr alloy, the design strategy followed an ICME approach to design, fabricate, and characterize as reported in [19]. Cu was added to improve the properties by solid solution strengthening [1,36], while Sc and Zr were added to form $\text{Al}_3\text{Sc}/\text{Zr}$ or $\text{Al}_3(\text{Sc},\text{Zr})$ stable precipitates. These precipitates are reported to provide heterogeneous nucleation sites, refining the microstructure to more equiaxed instead of columnar [5,39,41,46], and act as strengthening precipitates. Figure 1 provides an overview of CALPHAD-based, closed-loop approach employed for the design of the Al-Cu-Sc-Zr alloy. The approach is closed-loop in a sense that the computationally and analytical findings are validated with experiments. While our recent publications report the steps innate to this computationally-assisted closed-loop approach [19,47], the current paper is focused on the evaluation of the performance of the printed alloy by carrying out mechanical testing and microstructural characterization, along and across the build direction, in as-built and peak-aged conditions. The well-known anisotropy in AM builds is also explored, as it can open a lane for a range of demanding applications.

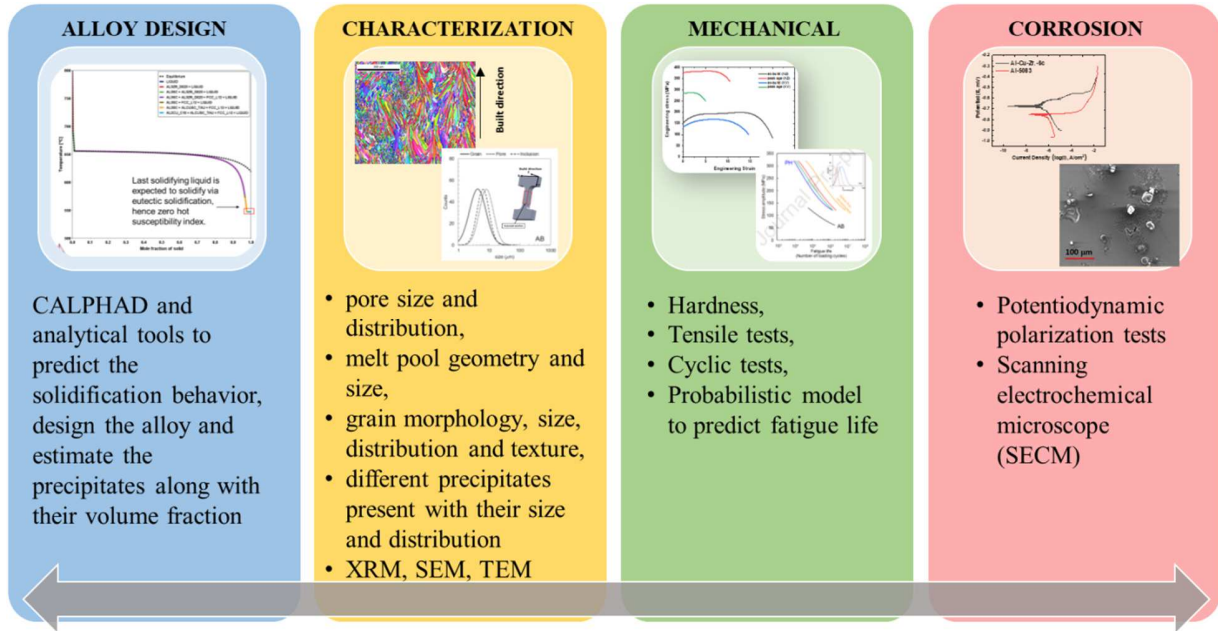


Figure 1. Overall approach for the current alloy Al-1.5Cu-0.8Sc-0.4Zr alloy for structural applications [19,47,48].

2. Experimental details

The samples for mechanical and microstructural characterization of the CALPHAD-designed Al-1.5Cu-0.8Sc-0.4Zr (wt.%) alloy were extracted from a printed block of dimensions $50(h) \times 25(w) \times 100(l)$ mm³. The effects of varying laser power (P , W) and laser scan speed (v , mm/s) were studied on microstructure and relative density [19]. $P = 350$ W, $v = 1000$ mm/s, slice thickness = 0.03 mm, and hatch spacing of 0.130 mm were the adjusted parameters to obtain a build that is as dense as possible with minimum defects. The experimental methods employed prior to printing can be found in [19].

Mechanical testing and microscopy of the Al-1.5Cu-0.8Sc-0.4Zr (wt.%) alloy were carried out to understand the structure-property relationship on XY (perpendicular to the build direction) and XZ (parallel to the build direction) planes of the build (Figure 2). Mini tensile samples were

machined with ~5 mm gauge length, ~1.2 mm thickness and ~1.25 mm gauge width, following standard ASTM A370 using CNC machine. The samples were then aged at 290°C for 20 hrs, at conditions optimized by Thapliyal et al. [19]. For each condition (as-built and aged), three tensile samples were machined from the XY planes and three from the YZ planes.

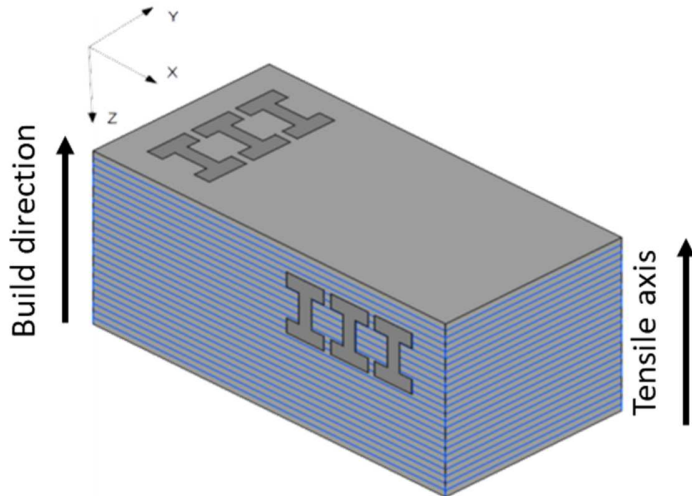


Figure 2. Location of extracted mini tensile samples for testing and microscopy from XY and XZ planes of the build.

To avoid surface defects, milled samples were ground to 4000 grit size using emery paper and then were polished to 1 μm surface finish by colloidal silica before testing. Mini tensile tests were carried out to fracture on an in-house built mini-tensile machine with a load cell capacity of 2000 N at room temperature and at an initial strain rate of 10^{-3} s^{-1} . Zeiss Xradia 520 Versa was used to perform X-ray microscopy (XRM). The primary objective was to study the effect of pores on tensile properties of specimens in as-built and peak aged conditions. A $3.75 \times 1.25 \times 1 \text{ mm}^3$ of gage volume was scanned from each condition. A 4X objective was used to acquire 2401 projections at a voltage of 50 kV and a current of 83 mA. Binning value, exposure time and voxel size were set to 2, 1 s and ~3.8 μm , respectively. Reconstruction of acquired projections was done to obtain a stack of images along the specimen height. Next, the stack of images was

processed with Dragonfly software to obtain 3D distribution of voids and their vol. % within the specimen. Care was taken while interpreting the pore volume % obtained by image analysis of the XRM image, as voxel size would determine the minimum resolvable pore size.

Scanning electron microscopy (SEM) was carried out on FEI Nova NanoSEM 230 on as-built and peak aged samples in XY and XZ planes. For microscopy, the samples were polished to 0.02 μm surface finish using colloidal silica. Imaging was performed in BSE mode; compositional analysis was carried out using the EDAX Octane Elite detector, whereas texture scans were obtained at a scan step size of 0.75 μm using the Hikari Super electron backscattered detector (EBSD). TSL OIM 8 software was used to analyze texture results. Fractography was done on all the samples, on both as-built and peak-aged conditions, in secondary electron (SE) mode.

Further, transmission electron microscopy (TEM) increased understanding of the presence and distribution of precipitates, especially at the melt pool boundaries. Foil for TEM study was milled carefully from the melt pool boundary of as-built and peak aged samples using FEI Nova 200 NanoLab Dual Beam Focused Ion Beam (FIB)/Field Emission Scanning Electron Microscope (FESEM) outfitted with platinum gun injection system (Pt GIS). TEM imaging and energy dispersive x-ray spectroscopy (EDS) analysis were carried out on FEI Tecnai G2 F20 S-Twin 200 keV FE-STEM.

3. Results

Detailed microscopy of samples mainly in the XZ direction is presented to elucidate the mechanical performance of the alloy.

Mechanical testing

Figure 3 shows engineering stress-strain curves for as-built and peak-aged tensile samples from both XY and XZ planes. There is an anisotropy observed for the samples machined from XY

plane that was parallel to the build layers and the samples from XZ plane consisting of several build layers. Figure 3 (a) gives tensile plots for the as-built condition for both the orientations, where samples machined from XY plane, show an improved ductility by almost 100% as compared to XZ direction with marginal improvement in strength. Interestingly, the peak-aged condition showed a drastic anisotropy for both strength and ductility where XY showed improved properties. For each orientation, peak-aging lead to improved strength, while ductility was sacrificed. Tensile properties for all four conditions are presented in Table 1.

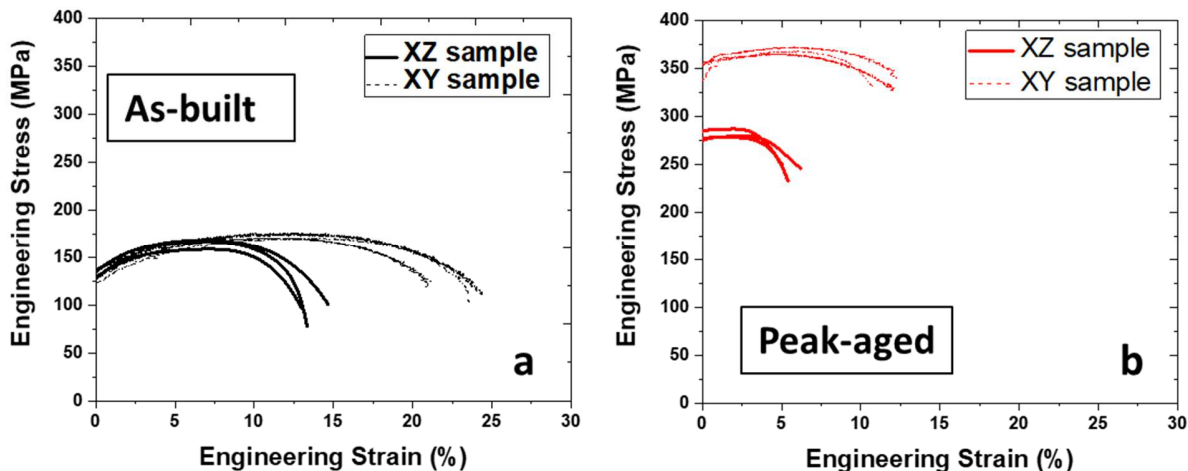


Figure 3. Engineering stress-strain curves for both orientations (a) as-built, and (b) peak aged condition.

Table 1. Tensile properties for different conditions of AM Al-1.5Cu-0.8Sc-0.4Zr alloy.

Samples	Heat treatment	YS (MPa)	UTS (MPa)	Elongation %
XY	as-built	150±3	195±5	23±1.5
XZ	as-built	140±8	170±2	13.5±1
XY	peak-aged	370±5	380±5	12.5±1
XZ	peak-aged	280±6	286±5	5.3±.2

Microscopy

Imaging and compositional analysis

Microscopy was carried out at different length scales to understand the mechanical behavior and to recognize ways to improve overall properties and thus alloy performance. 2D slices from the 3D reconstructed images of as-built and peak-aged samples are presented in Figures 4 (a) and (b), respectively. The scanned volumes exhibited no internal cracks. However, spherical porosity and lack of fusion defects were observed. Figures 4 (c) and (d) show the distribution of pores within the scanned volume of as-built and peak-aged samples, respectively. For the as-built sample, pore volume % of $\sim 1.16 \pm 0.34$ % was obtained by image analysis of XRM data; whereas for the peak-aged condition, the pore volume % of $\sim 0.86 \pm 0.33$ % was obtained. Pores of average diameter greater than 7–8 μm were resolved, as reported by Haridas et al. [47] for the same alloy.

Figure 5 presents the micrographs from SEM in BSE mode. Figures 5 (a) and (b) are from the as-built condition, where Figure 5(a) is the micrograph at low magnification covering around 5-6 melt pools. With an increase in magnification, as shown in Figure 5(b) covering a single melt pool, there is no evidence of precipitates or change in contrast due to the second phase at the SEM level. For the peak-aged condition, segregation of bright spots along the melt pool boundaries and along the columnar grain boundaries (Figures 5 (c) and (d)) is apparent. SEM-EDS mapping (Figure 5 (d)) revealed these bright spots as Cu-rich regions (Figures 5 (d₆)) with no evidence of precipitation due to Sc and Zr. To further investigate and confirm the location of the precipitates, TEM foils were milled from the melt pool boundary for both as-built and peak aged samples, indicated by a yellow box in Figure 5 (b) and (d), respectively.

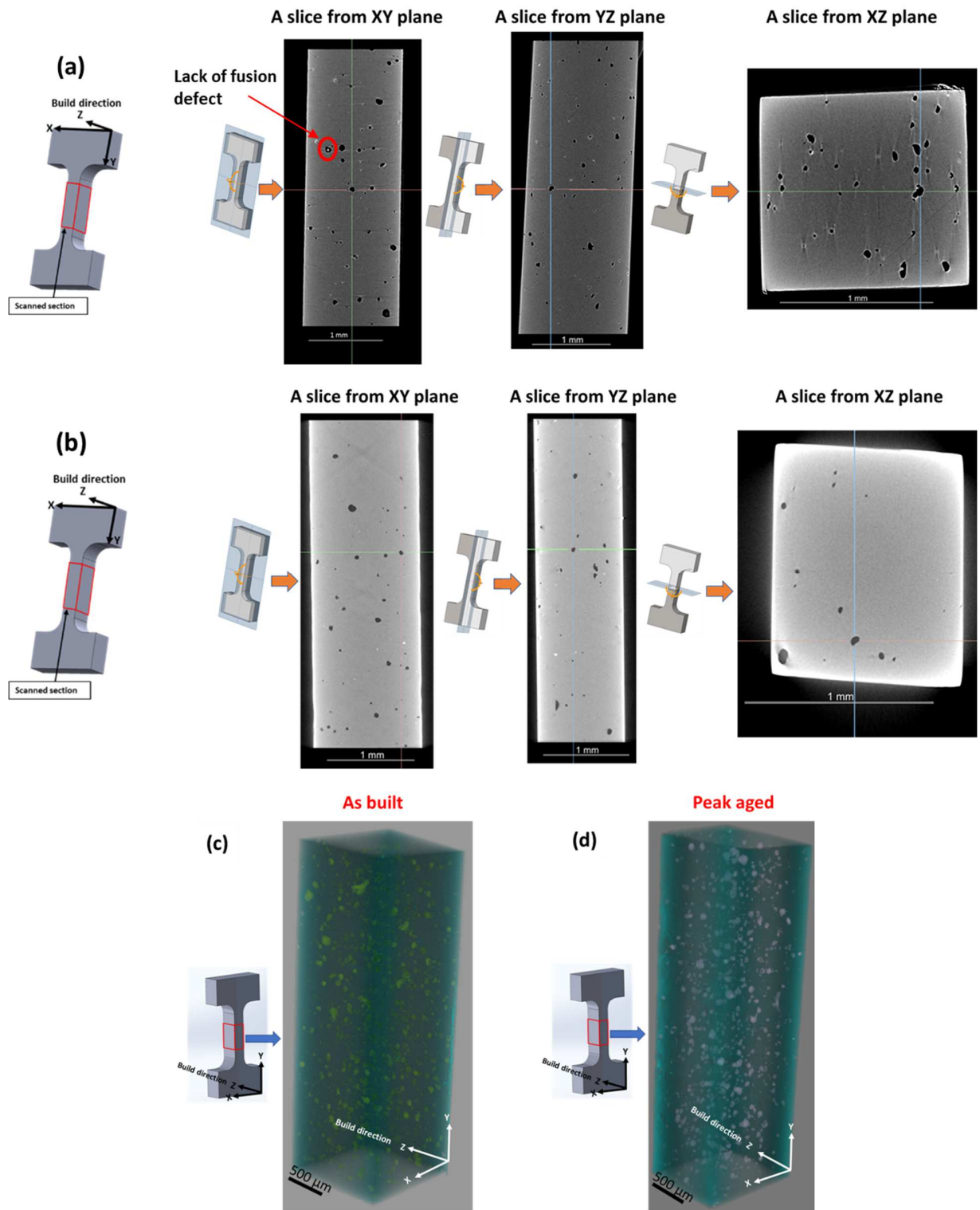


Figure 4. Example of 2D slices from within the gauge of a mini-tensile sample in (a) as-built condition, and (b) peak-aged condition. 3D distribution of defects within the gauge of a mini-tensile sample in (c) as-built condition, and (d) peak-aged condition.

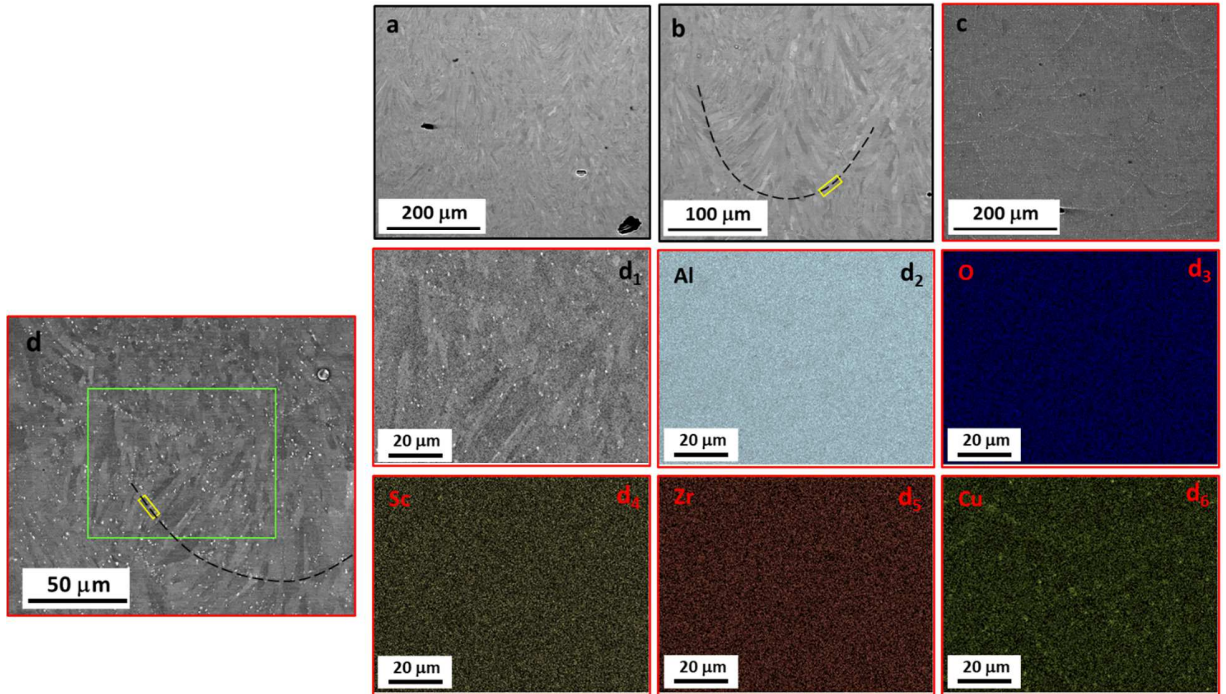


Figure 5. Micrographs from SEM in BSE mode, (a) low-magnification image of the as-built condition with 5-6 melt pools, (b) a higher magnification image of the as-built condition to cover a single melt pool, (c) low-magnification image of the peak-aged condition, and (d) high-magnification image of peak-aged condition. The region enclosed in the green rectangle is where EDS mapping for composition analysis is carried out. (d₁) SEM-BSE image for peak-aged condition, (d₂) Al (light blue), (d₃) O (navy blue), (d₄) Sc (yellow), (d₅) Zr (red), and (d₆) Cu (green). **Note:** Dotted line indicates the melt pool boundary and the yellow box is the region where TEM foil was milled.

Figure 6 shows the STEM images and EDS mapping for the peak aged condition. Figure 6 (a) is the low-magnification STEM image from near the melt pool boundary with equiaxed and columnar grains (partially visible), while Figures 6 (b) and (c) are images at higher magnification. Bright spots are observed at the grain boundary and triple junctions whereas light contrast precipitates are observed along the grain boundaries. Figure 6 (c) clearly shows feather-type features emanating from the grain boundaries towards the grain interior, also seen in Figures 6 (a) and (b). The STEM-EDS mapping shown in Figure 6 (d) confirmed the bright precipitates to be Cu-rich and depleted of Al (Figures (6 (d₁) and (d₅))), around 50–100 nm in size. The

precipitates in lighter contrast along and at the grain boundaries are confirmed to be Al-Sc and Al-Sc-Zr (Figures 6 (d₃) and (d₄)), with size ~25 nm and the average spacing between the precipitates to be ~20–40 nm. The EDS map for Oxygen in Figure 6 (d₂) does show high-intensity spots but it is difficult to relate any feature when compared with STEM image in Figure 6 (d).

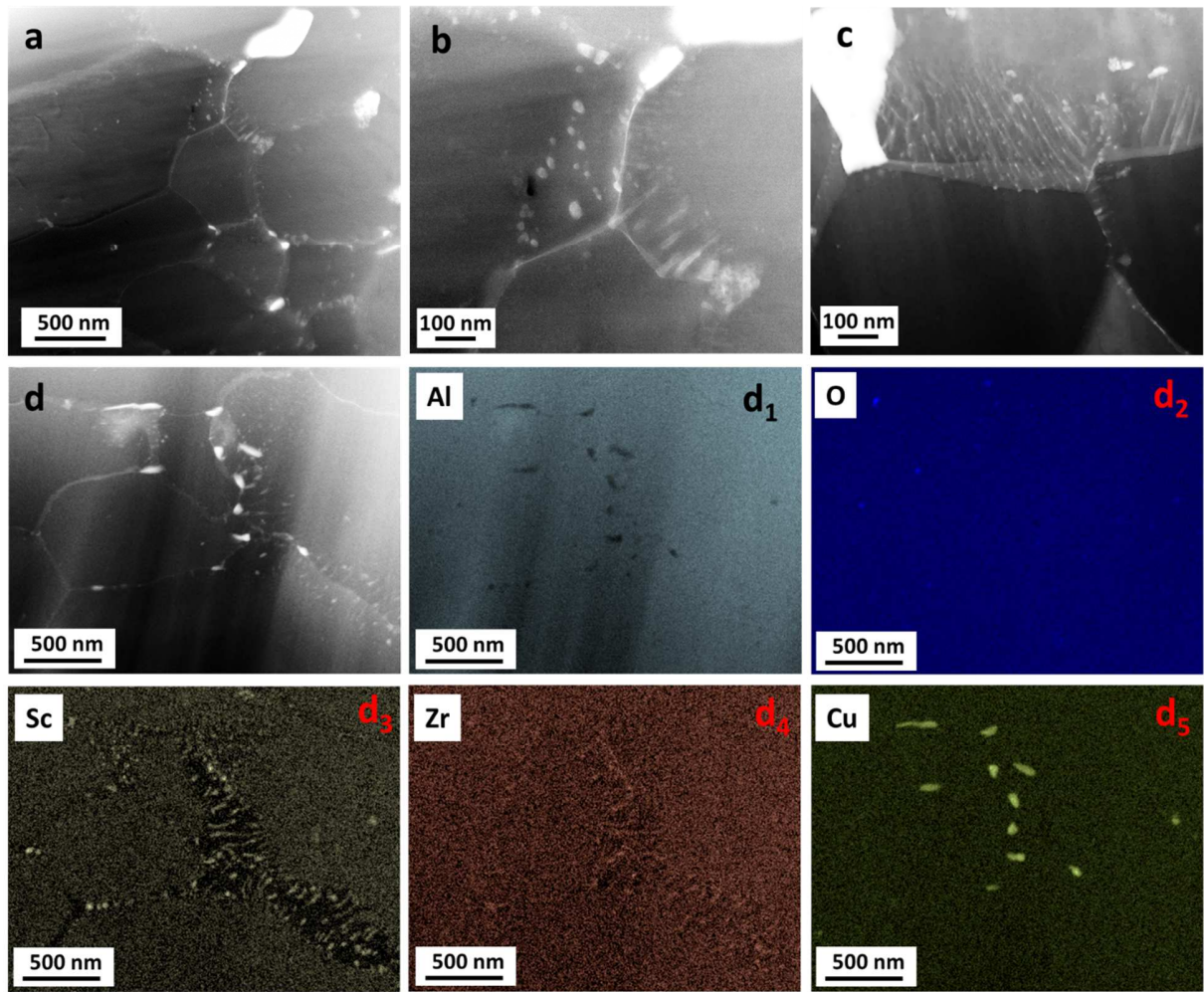


Figure 6. Imaging in STEM mode for the peak-aged sample. (a) Micrograph with columnar and equiaxed grains. The dark contrast is from the matrix, whereas the bright contrast is from the precipitates, (b) magnified image of (a) imaging precipitates along the grain boundaries in bright contrast with an average size of ~25, (c) magnified image showing *feather*-type features accompanied by precipitates along the grain boundaries in bright contrast. STEM-EDS map: (d) STEM image, (d₁) Al map in light blue, (d₂) O map in navy blue, (d₃) Sc map in yellow, (d₄) Zr map in red, and (d₅) Cu map in green.

Traditional TEM diffraction studies were carried out to look for precipitates inside the grain, if any, and obtain precipitate structure and dislocation morphology in peak aged condition (Figure 7). Figure 7 (a) gives a low magnification bright field image of the TEM foil showing equiaxed and columnar grains. Figure 7 (b) is a weak-beam bright field with Bragg's condition appropriate to image the dislocations, $B = [110]$, $g = \bar{1}\bar{1}\bar{1}$. The image is a magnified view of the highlighted grain in Figure 7 (a) where precipitates are observed in dark contrast inside the grains. Figures 7 (a) and (b) confirm precipitates decorating and pinning the dislocation line length. Figure 7 (c) gives the diffraction pattern for [001] zone axis with superlattice spots (encircled in yellow), confirming the presence of precipitates with $L1_2$ crystal structure. Figures 7 (d), (e) are weak-beam dark field and bright field images, respectively, with $g = \bar{1}00$, imaging the $Al_3Sc/Al_3(Sc,Zr)$ precipitates of ~ 5 nm in size within the grain, and the average spacing between the precipitates ~ 10 nm. Figure 7 (f) is a two-beam bright field image with $g = 200$ where the coherent strain field contrast is observed around the precipitates, confirming the $Al_3Sc/Al_3(Sc,Zr)$ precipitates to be coherent with the matrix. The location, size, and type of precipitates for the peak-aged condition are listed in Table 2.

After a detailed TEM study for peak-aged condition, the as-built condition was also studied for comparison and is presented in Figure 8. Figures 8 (a) and (b) gives a two-beam bright field image showing bigger dark precipitates heterogeneously distributed whereas smaller grey precipitates homogeneously present in the matrix. Figure 8 (c) shows the presence of high dislocation density when compared with the peak-aged condition (Figure 7 (b)) and confirms the pinning of dislocations by precipitates. Figure 8 (d) is a STEM image with a location similar to the red enclosure in Figure 8 (a) where bright precipitates in STEM are the precipitates in dark contrast in bright field mode, Figure 8 (a). The same location is then taken for EDS study as seen

in Figure 8 (e), where the bright precipitates in STEM mode are confirmed to be Cu-rich (Figure 8 (e₅)). When compared with the peak-aged condition, there is no evidence of Sc or Zr rich precipitates at or along the grain boundaries (Figures 6 (d₃) and (d₄)).

On comparison of as-built and peak-aged conditions:

- a) The as-built condition has a high dislocation density.
- b) With aging, there is evidence of Sc and Zr rich precipitates at and along the grain boundaries.
- c) The as-built condition has Cu-rich regions aligned inside the grains whereas aging leads to coarsening of Cu-rich regions detected at grain boundaries and triple junctions.

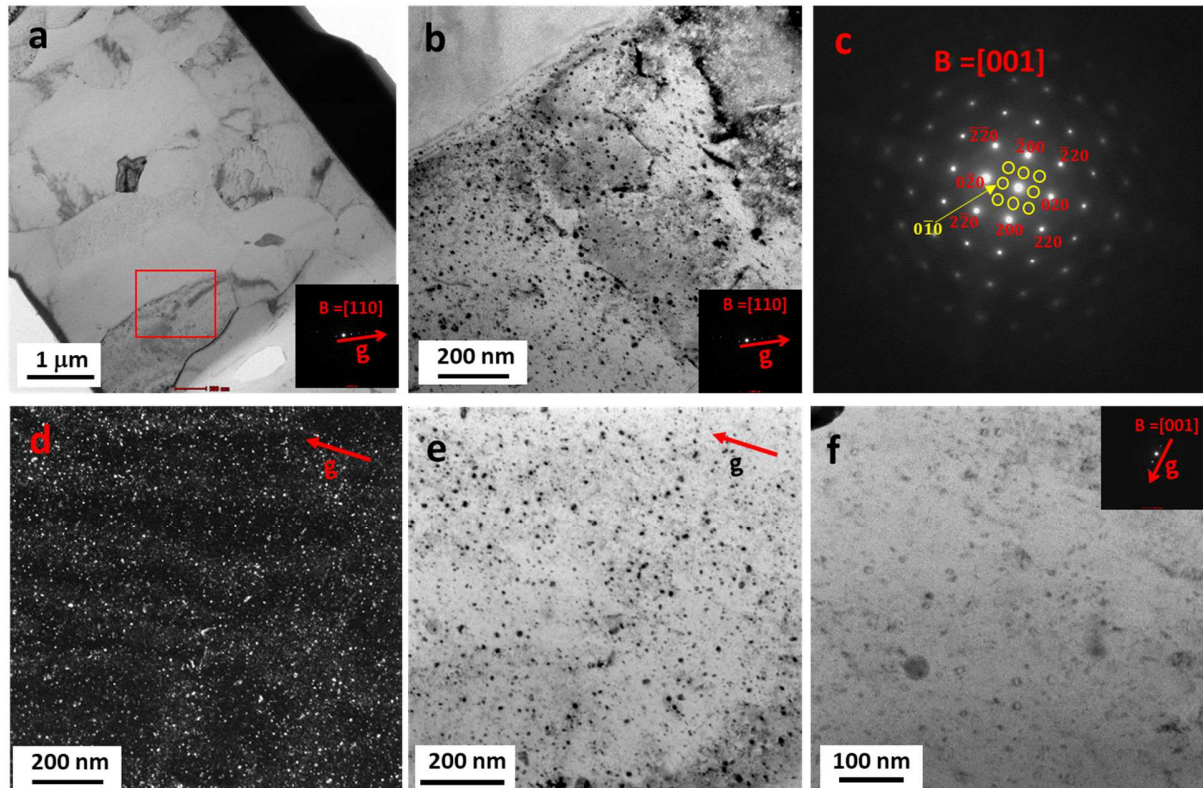


Figure 7. TEM imaging of peak aged specimen. (a) low magnification weak-beam bright field, $B = [110]$, $g = \bar{1}1\bar{1}$, (b) weak-beam bright field showing the precipitates along the dislocation length, $B = [110]$, $g = \bar{1}1\bar{1}$, (c) Diffraction pattern from [001] zone axis with $L1_2$ superlattice spots (encircled in yellow), (d) weak-beam dark field from with $g = \bar{1}00$ in (c), (e) weak beam bright field with $g = \bar{1}00$ in (c), and (f) two-beam bright-field image showing coherent strain-field contrast around precipitates, $g = 200$.

Table 2. Precipitate type, location, size, and average spacing obtained from TEM analysis in the aged condition.

Type of precipitates	Location	Size (nm)	Average spacing (nm)	Mode
Cu-rich regions	at the grain boundaries	~50-100	NA	SEM-EDS, STEM-EDS
$\text{Al}_3\text{Sc}/\text{Al}_3(\text{Sc},\text{Zr})$	along the grain boundaries	~25	~20-40	STEM-EDS
$\text{Al}_3\text{Sc}/\text{Al}_3(\text{Sc},\text{Zr})$	within the grain	~5	~10	TEM-Diffraction

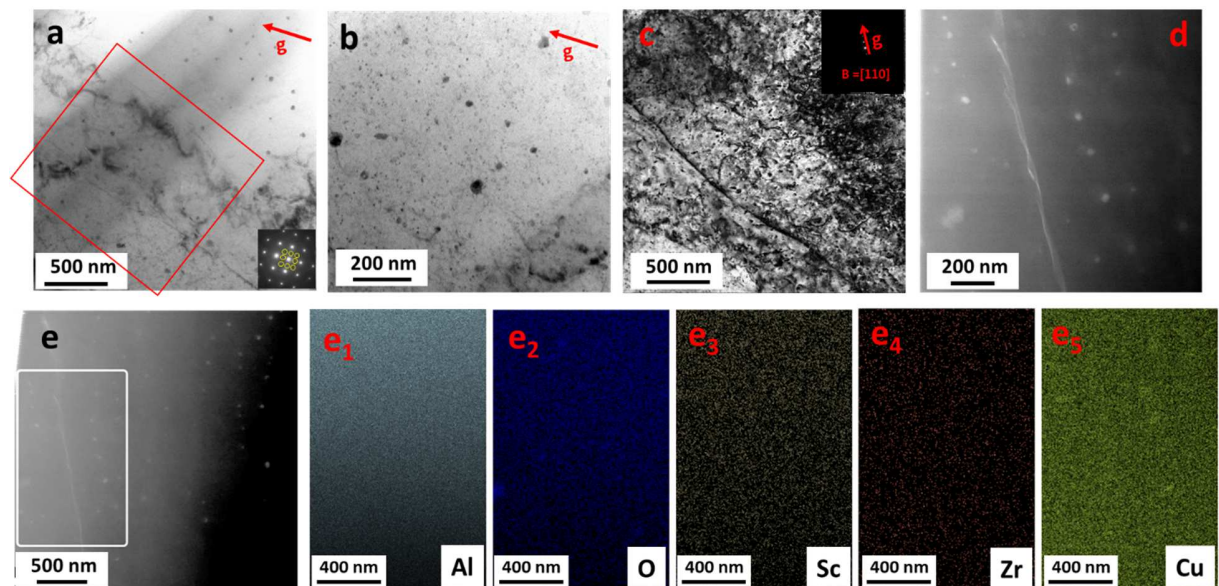


Figure 8. TEM imaging in as-built condition. (a) weak-beam bright field showing the precipitates of different contrast in the matrix, $B = [001]$, $g = 0\bar{1}0$, (b) high-magnification two-beam bright field image, $B = [001]$, $g = 0\bar{1}0$, (c) weak-beam bright field from with $B = [110]$, $g = 1\bar{1}\bar{1}$, STEM-EDS map: (d) STEM image, STEM EDS (e) STEM image, (e₁) Al map in light blue, (e₂) O map in navy blue, (e₃) Sc map in yellow, (e₄) Zr map in red, and (e₅) Cu map in green.

Texture

Texture studies were carried out for as-built and peak aged conditions, in-build direction, to understand the possible reason for the equiaxed to columnar transition. Figure 9 gives the results from texture studies for as-built sample in the XZ plane, where the build direction for Figures 9 (b-d) is from right to left. Figure 9 (a) is a 3D depiction of the build using OIM micrographs,

giving the orientation information of different planes. Figure 9 (b) is an orientation image map (OIM), where the melt pool boundaries are marked with broken black lines. The corresponding pole figure is presented in Figure 9 (c). The melt pool is textured, where the columnar grains are orientated for or near $\{001\}$. The equiaxed grains at near the melt pool boundaries and in regions where melt pools coincide (marked in black solid circles), appear to have near $\{111\}$ orientation. Figure 9 (d) is a grain aspect ratio map where aspect ratio ≥ 2 is assigned to columnar grains, whereas <2 is assigned to equiaxed/near equiaxed grains. Columnar grains, blue in color, are observed within the melt pool with a fraction of 0.72. The green color assigned to equiaxed/near equiaxed grains is present near the melt pool boundaries and between the two melt pools in the direction parallel and perpendicular to the build direction, with a fraction of ~0.28. Figure 9 (e) shows the Kernel average map (KAM) and sheds light on the extent of residual strain in the sample. The KAM map is shown to 2° misorientation with 5 divisions. The KAM map exhibits more blue regions, i.e., stress-relieved grains, near the melt pool boundaries as compared to within the melt pool.

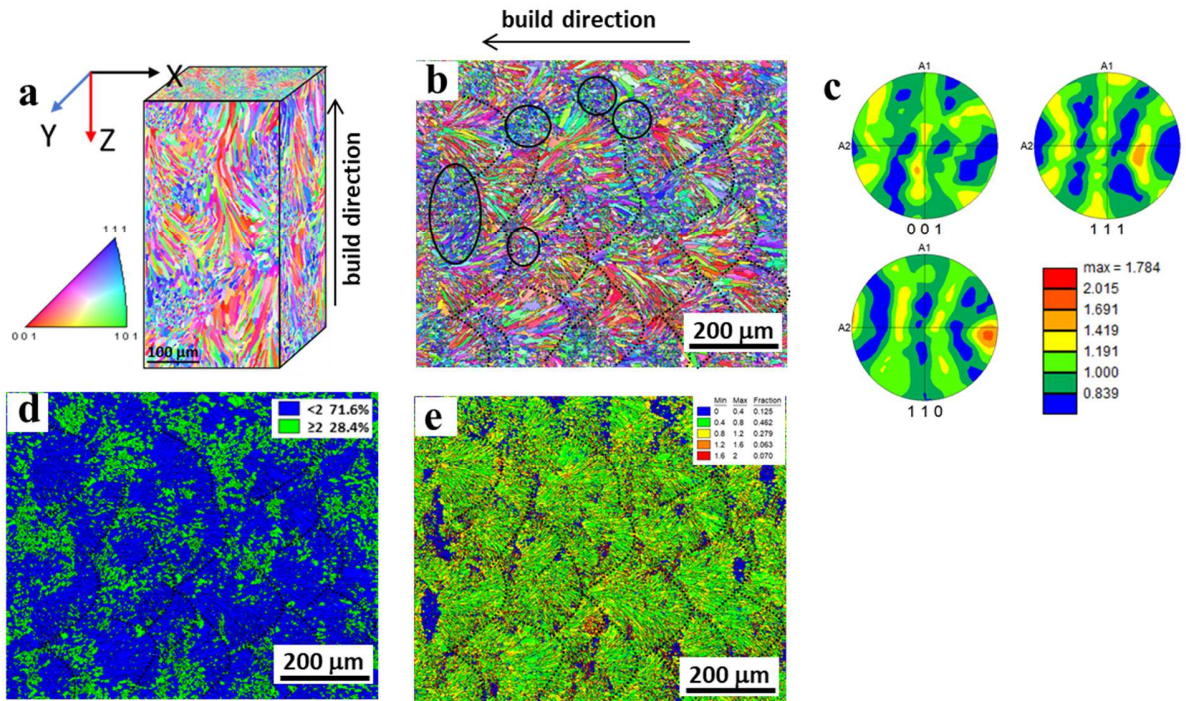


Figure 9. Texture analysis in-build direction for as-built sample: (a) 3D depiction of the build using OIM micrographs, (b) an OIM, (c) pole figure corresponding to b, (d) the grain shape aspect ratio map (GSAR) sorting the equiaxed and columnar grains on the basis of aspect ratio, and (e) the KAM map. **Note:** the build direction in (b), (d), and (e) is horizontal, running from right to left.

Figure 10 gives the texture information in the XY plane, perpendicular to the build direction, for the as-built sample. XY plane gives the projected image of the melt pool and thus the columnar and equiaxed grains. The {100} orientation (in red) is the melt pool, whereas the {111} orientation (in blue) is actually the melt pool boundary (Figure 10 (a)), and the magnified image is shown in Figure 10 (b). The transverse section seems to have a random texture unlike the section parallel to the build direction (comparing Figures 9 (a) and 10 (a)) and as seen from pole in Figure 10 (c). Figure 10 (d), the grain aspect ratio map of the projected image, shows an increased apparent ratio of equiaxed to columnar grain morphology.

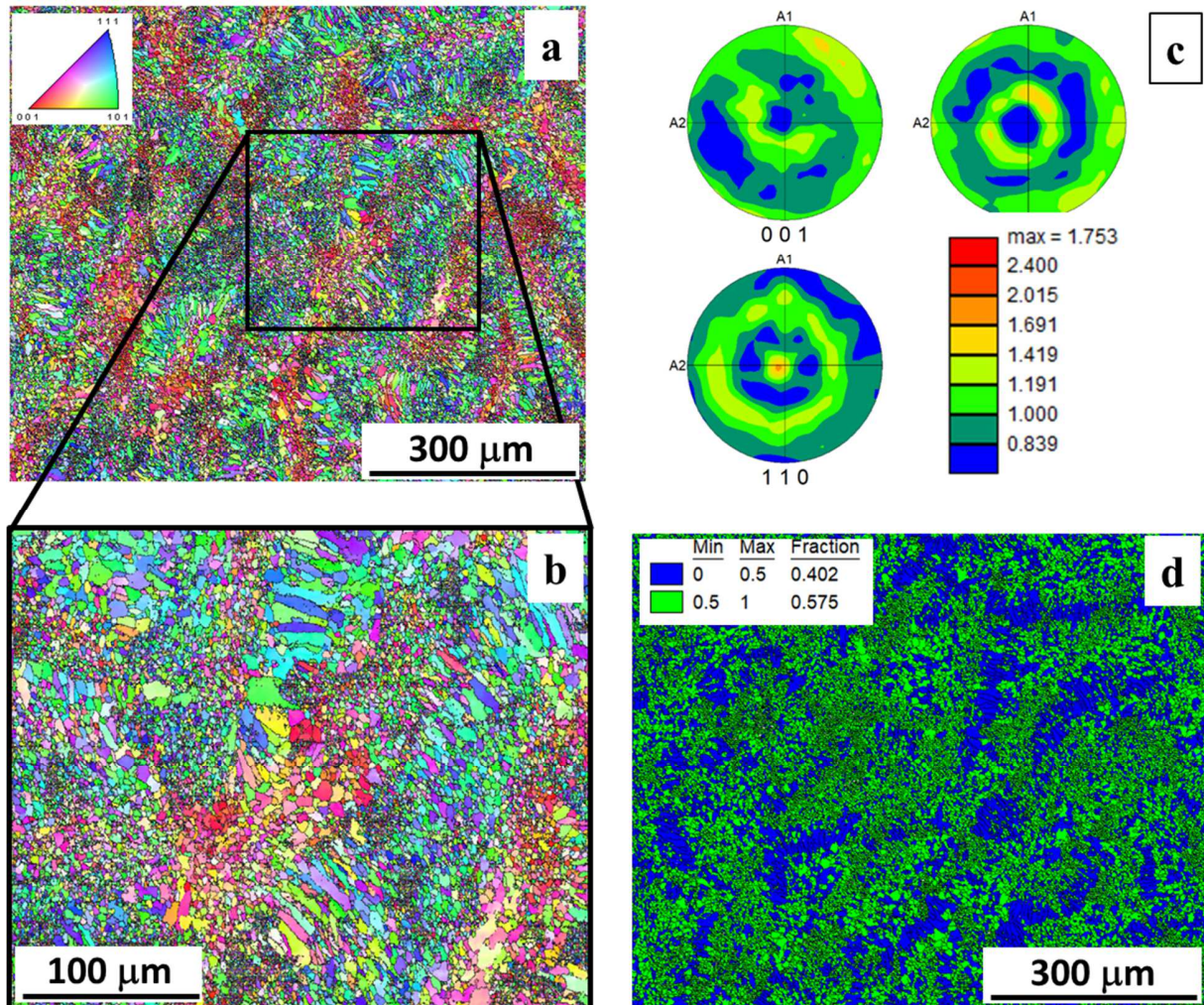


Figure 10. Texture analysis for as-built sample in XY plane. (a) an OIM superimposed with an image quality (IQ) map, (b) magnified view of (a), (c) pole figure corresponding to (a), and (d) a GSAR map - equiaxed and columnar. **Note:** Build direction is inside the plane

Figure 11 presents micrographs for the peak-aged sample in XZ plane. Figures 11 (a) and (b) gives the orientation information showing a similar texture as the as-built sample (Figures 9). The melt pool with sky blue color, where one vertical half of the melt pool has columnar morphology; whereas the other half is with equiaxed grain morphology, a similar observation as for as-built condition. The 67° inter-layer rotation scan-strategy is believed to cause change in a) the direction of maximum thermal gradient between the layers [49], and b) the angle between

growth direction and scanning direction between the layers (consequently changing growth rate) [50] . Such scan strategy is believed to result in change in grain morphology, bending of columnar grains or change in grain orientation.

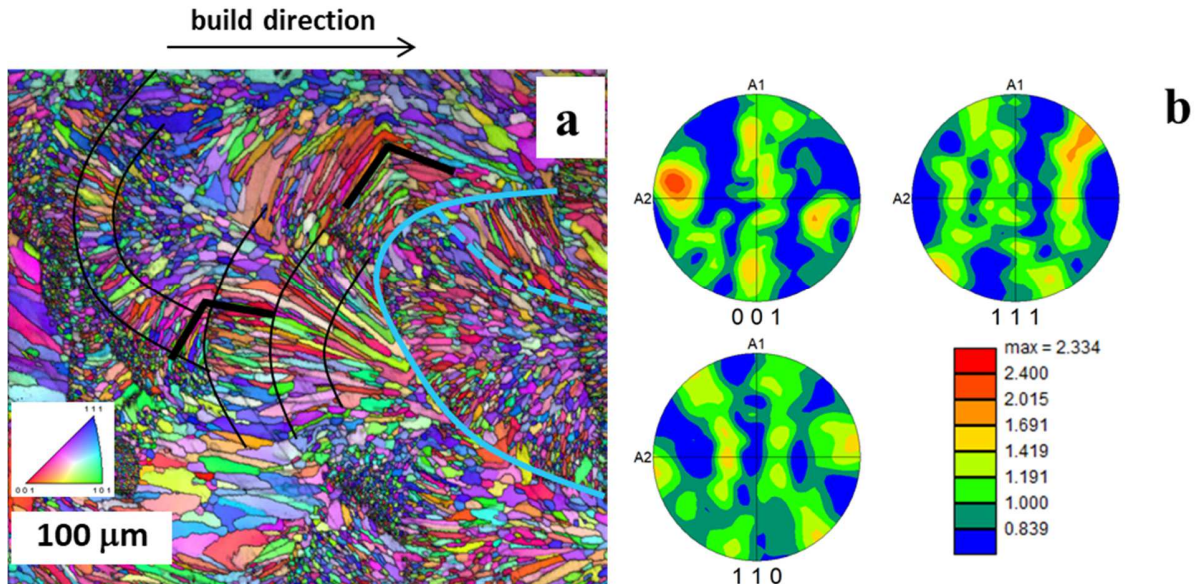


Figure 11. Micrographs in XZ plane for peak-aged sample. (a) an OIM superimposed with IQ map – showing bending and breaking of columnar grains, and (b) pole figure corresponding to (a). **Note:** the build direction is horizontal, running from left to right

Fractography

Figure 12 shows detailed fractography for as-built and peak-aged samples on XZ and XY planes in secondary electron (SE) mode in SEM. Figures 12 (a)–(c) are micrographs from as-built samples tested in tension to fracture, where Figure 12 (a) is from XZ plane, in the build direction. Figure 12 (a) shows a **wavy** surface after deformation. Around 4–5 melt pools are observed where the cracks/grown voids are noticed along the melt pool boundaries. The slip lines propagate across the columnar grains. Figure 12 (b) gives the macrograph in the XY plane, showing dimples. Also, the fractured surface is noticeably smaller in area (bound by a broken black line) as compared to the undeformed region (bound by a solid black line). Defects such as debris from the fracture are encircled in yellow; whereas fusion defects, are encircled in green.

The features encircled in red do not seem to correspond to a pore, as the pore size from XRM is $\sim 7\text{--}8 \mu\text{m}$, which is smaller than this feature, $\sim 30\text{--}70 \mu\text{m}$. This feature seems corresponding to the apex of the melt pool boundary where all the columnar grains of different orientations meet (enclosed by a red circle in Figures 12 (a)). Figure 12 (c), magnified view of fractography from Figure 12 (b), features a fractured lip with slip lines transferring across the columnar grains. Figures 12 (d)–(f) are micrographs from the peak-aged fractured samples. Figures 12 (d) and (e) are micrographs from the XZ plane, whereas Figure 12 (f) is from the fractured surface, XY plane. Figure 12 (d) is a low-magnification micrograph with the near-fractured end to the right. Note that the deformation is considerably less as one travels away from the fractured surface (Figure 12 (d)), deduced by less wavy surface and fewer slip lines being observed. Figure 12 (e) is a high-magnification micrograph at and near the fractured surface, focusing on a single melt pool. The precipitates appear in bright contrast as dots. Clearly, the slip lines emerge from a columnar boundary, travel a columnar grain and get inhibited by the adjacent columnar boundary. Each columnar grain has a set of slip lines oriented in the same direction. Different columnar grains are observed with a different set of slip systems being activated as per the orientation. The angle between the set of slip lines in the consecutive columnar grains is $\sim 70^\circ$. The melt pool boundary is tracked by a broken red line, with no sign of crack at the boundary or columnar grain boundary, and the observation is supported by a low magnification image (Figure 12 (d)). The apex of the melt pool is enclosed by the red circle that seems to be the site for crack nucleation, with no sign of slip lines. Figure 12 (f) is the fractured surface showing from the difference in the cross section of fractured and grip area, enclosed by broken and solid black lines, respectively.

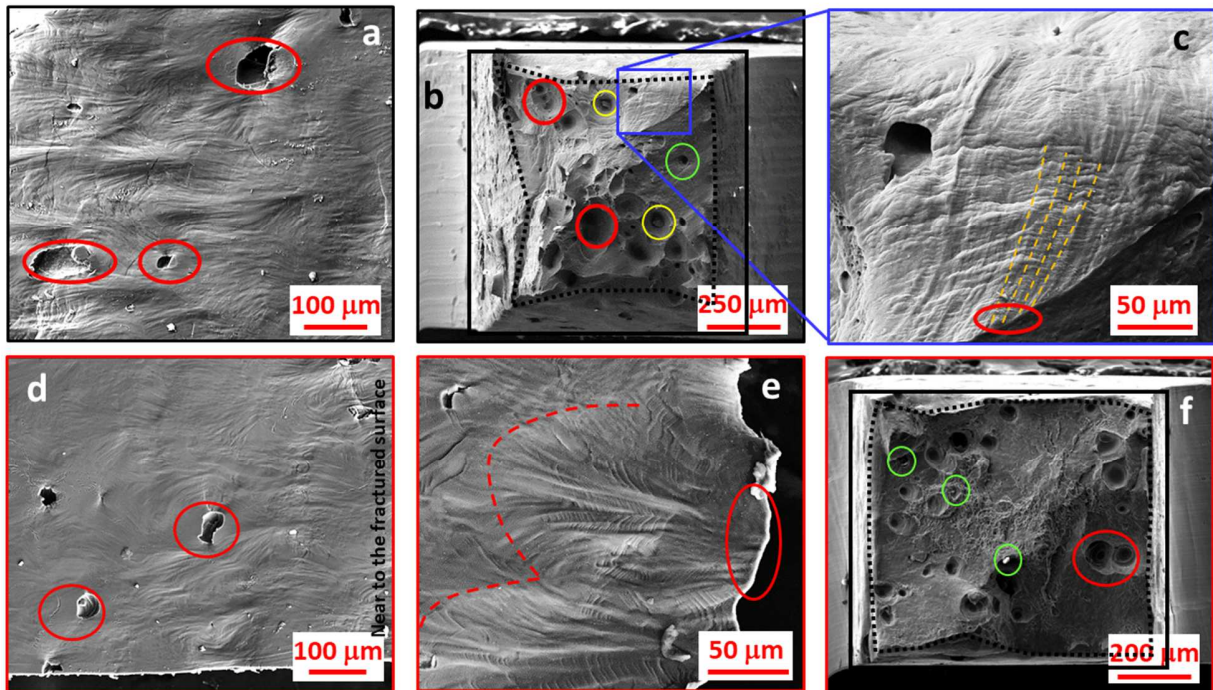


Figure 12. Fractography in SE mode. **As-built condition** (a) low-magnification micrograph showing XZ plane with cracks at the melt pool boundary and slip lines transferring across the columnar grains, (b) low-magnification fractography in XY plane with ductile fracture, unfused regions (green), debris (yellow), melt pool apex (red), (c) magnified image from (b) to point out the slip transfer across the columnar grains where columnar grain boundaries are traced by broken orange lines. **Peak-aged condition** (d) low-magnification micrograph showing ~4–5 melt pools in XZ plane (e) high-magnification image showing slip lines within the columnar grains that are inhibited by the columnar grain boundaries in XZ plane, and (f) fractograph in XY plane showing mixed ductile-brittle fracture mode. **Note:** Images with black border correspond to the as-built condition and with red border correspond to the peak-age condition.

4. Discussion

The current study is focused on understanding the aspects of mechanical properties through detailed microstructural characterization at different length scales. Efforts were made to understand the microstructure via grain size and morphology, phases present, crystallographic orientation, and fractography; and extend the knowledge to attempt for a higher fraction of equiaxed structure, thus leading to improved performance of the alloy.

XRM study revealed no internal cracks with pore volume ~1% (Figure 4), which indicates good

printability, as predicted by Thapliyal et al. [19,20] via Scheil-Gulliver solidification simulations for the current alloy. The experimental studies carried out by DebRoy et al. [15], Schmidtke et al. [17], and Qbau et al. [35] on the addition of Sc to the AM Al alloy lead to similar conclusions of achieving a crack-free build.

Further testing the alloys in both the orientations an anisotropy was observed as seen from Figure 3. As discussed in the review on anisotropy in various additively manufactured systems by Kok et al. [51], the anisotropy is attributed to factors such as grain morphology, crystallographic orientation, lack of fusion defects, layer banding, etc. The XZ plane consists of several build layers where the stress axis is near parallel to the columnar grain boundaries, spanning multiple melt pools and printed layers, with near {100} orientations (Figures 2, 5, 9, and 11). From Figure 12 (a) and (d), with the melt pool apex confirmed as the crack nucleation site, the columnar grains give an easy path for slip transfer, and the crack propagates easily along and across the columnar grain, due to the orientation and morphology. A similar observation is reported in the literature by Aboulkhair et al. [6] where melt pools' detachment is reasoned for the anisotropy when tested in the build direction. On the other hand, samples in the XY plane consist of a cross-section of melt pools (Figure 10) and thus a higher grain boundary area and increased strength via Hall-Petch relation [52].

The peak-aged condition showed improved strength while sacrificing ductility in both the orientations (Figure 3 and Table 1) and pronounced anisotropy. This is due to the formation of precipitates at the grain boundaries, along the grain boundaries and within the grain interiors, confirmed via SEM and TEM (Figures 5–8). SEM-EDS analysis for peak-aged condition revealed the Cu-rich regions decorating the melt pool and at columnar boundaries (Figures 5–7) and $\text{Al}_3\text{Sc}/\text{Al}_3(\text{Sc},\text{Zr})$ with the L1_2 crystal structure established along the boundaries and within

the grains (Figures 6–7).

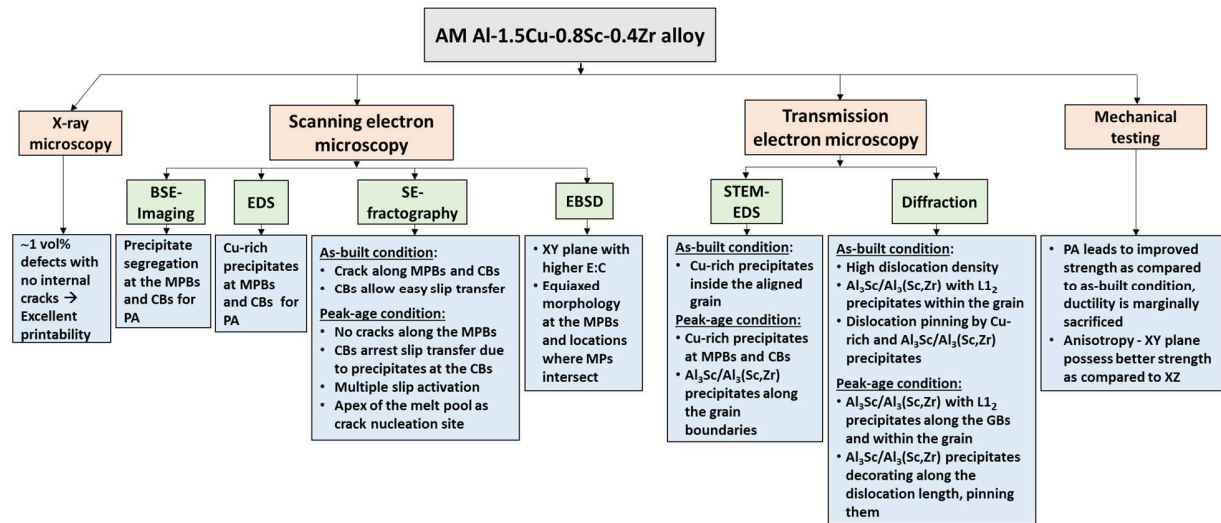
Due to the similarity of the FCC matrix and L₁₂ structure of the Al₃Sc/Al₃(Sc/Zr) precipitates the lattice misfit is minimum, and hence these precipitates act as effective seeds [38]. Consequently, the Al₃Sc/Al₃(Sc,Zr) precipitates provide heterogeneous nucleation sites leading to a more refined structure. Spierings et al. [38,39] reported a similar observation, where the addition of Sc and Zr to Al-Mg alloy leads to a bimodal microstructure. Apart from acting as seed precipitates, Al₃Sc/Al₃(Sc,Zr) pin the dislocations and thus hinder their movement as also reported in the literature [38,39]. The coherent nature of the precipitates (Figure 7 (f)) leads to an increase in the strain energy and increase in strengthening as shown by Marquis et al. [53] for Al₃Sc precipitates in Al-Sc alloy. Microstructural characterization and computational work [19] showed that the precipitates are stable and do not coarsen with aging, which is an important result for long-term applications. Thus these L₁₂ coherent precipitates act as both seed and strengthening precipitates. The Cu was added in the alloy with the aim to improved solid solution strengthening as in 2XXX wrought alloys. The addition of Cu leads to Cu-rich regions which could be Al₂Cu as reported by Chen et al. [36] in Al-Cu-Sc alloy and confirmed from CALPHAD calculations carried out for the current alloy by Thapliyal et al. [19]. The TEM results as shown in Figures 6 (d₅) and (d₁) do confirm Cu-rich regions but to be lean in Al. Following Spierings et al. [38,39] work, the STEM-EDS map was expected to show oxides in the system. As shown in Figure 6 (d₂) there are high-intensity spots for O EDS map but it is difficult to relate to any feature when compared with Figure 6 (d). The Cu-EDS map does show Cu in the matrix too, which leads to the conclusion that Cu addition leads to an increase in strength via both solid solution strengthening and precipitate strengthening. With peak aging due to Cu-rich and Sc-Zr rich precipitation, slip transfer across the columnar grains is restricted leading to the activation of multiple <111> slip

systems as seen in Figure 12 (e); thus no cracks are observed along the melt pool boundaries (Figure 12 (d)).

As the sample is processed via additive manufacturing involving rapid solidification, a high total dislocation density (mobile and immobile) of the order of $10^{13}\text{--}10^{14}\text{ m}^{-2}$ is expected, as reported by Aboulkhair et al. [6] in the review of AM Al alloys. Wang et al. [54] found the origin of this high density of dislocations is due to localized heating and cooling cycles during laser beam scanning. The dislocations are observed to be pinned by both precipitates although the dislocation density is as-built is higher than peak-aged condition (Figures 8 (c) and 7 (b)). The absence of precipitates and higher dislocation density, makes the as-built condition more ductile, as seen from the wavy deformed surface (Figure 12 (a)) and dimples observed in the fractured surface (XY plane) (Figure 12 (b)). The conclusion is that slip transfer restriction across the columnar grains is due more to precipitates at the boundaries than to texture.

During the LPBF process, the laser scans the powder bed, and the orientation between the consecutive layers being 67° aims to break the columnar morphology [55]. Solidification will first lead to the nucleation of seed precipitates acting as heterogeneous nucleation sites to form finer equiaxed grains. Solidification transition will take place from equiaxed grains to columnar by epitaxial growth. With 67° inter-layer rotation scan-strategy, the direction of maximum thermal gradient and the angle between scanning direction and growth direction also changes [49,50]. This scan-strategy is believed to disrupt the selective growth direction, as is also seen in Figure 9 (b). This leads to a change in the orientation of epitaxially grown columnar grains in $\{100\}$ in the case of FCC. This is also the reason for the bending of columnar grains and almost vertical half of the melt pool shows columnar grains; whereas the remaining half consists of more near-equiaxed grains (Figures 9 and 11).

Thus, tailoring the properties by understanding solidification has proved to improve the understanding of the grain size, grain morphology, grain orientation, and the phases present. This leads to a successful defect-free, printable material with good performance for a specific application, summarized in Figure 13. This alloy has proved to be a potential candidate to date in AM Al alloys with excellent properties.



*AB=as-built, PA=peak aged, CB=columnar boundary, MPB=melt pool boundary, MP=melt pool, GB=grain boundary, E:C=equiaxed to columnar grain morphology ratio

Figure 13. Summary of the present work with key results and takeaways.

Conclusions

The present study analyzed and compared the microstructure and deformation response of as-built and peak-aged conditions of a novel AM Al-1.5Cu-0.8Sc-0.4Zr alloy, processed by LPBF.

- X-ray microscopy revealed no internal cracks with defects volume ~1% indicating the alloy with excellent printability.
- Anisotropy is observed for both conditions, pronounced in peak-age condition, where samples perpendicular to the build direction showed improved properties.
- The peak-aged samples exhibited greater strength (~380 MPa) as compared to as-built in XY orientation while ductility was sacrificed marginally.

- The improvement in tensile properties with aging is attributed to a) coherent L1₂ Al₃Sc/Al₃(Sc,Zr) precipitates leading to a more refined equiaxed microstructure and improved strength by acting as seed and strengthening precipitate, and b) Cu-rich regions contributing to the strength via solid solution and precipitate strengthening.
- As observed from fractography, the columnar grains in as-built condition allow easy slip transfer with the apex of the melt pool acting as the nucleation site. This weakening is overcome in the peak-aged condition by precipitation of new phases at the columnar and grain boundaries.

Acknowledgments

The work was sponsored by the Office of Naval Research (ONR) under the ONR Award #N00014-17-1-2559. The authors thank the Materials Research Facility (MRF) and Advanced Materials and Manufacturing Processes Institute (AMMPI) at the University of North Texas for access to the microscopy facilities. The authors also thank Amalia Siller and Patrick Toll for preparing the samples for testing and microscopy.

Declaration of Interest

None.

Author contributions

P.A. S.G. and R.S.M. designed the research. P.A. S.G. S.T. S.S. performed testing and microscopy at different levels. R.S.H. helped in machining the samples. P.A. S.G. and R.S.M analyzed the results. P.A and R.S.M. drafted the manuscript. All authors contributed to the final manuscript.

References

- [1] D. Herzog, V. Seyda, E. Wycisk, C. Emmelmann, Additive manufacturing of metals, *Acta Mater.* 117 (2016) 371–392. <https://doi.org/10.1016/j.actamat.2016.07.019>.
- [2] D.D. Gu, W. Meiners, K. Wissenbach, R. Poprawe, Laser additive manufacturing of metallic components: Materials, processes and mechanisms, *Int. Mater. Rev.* 57 (2012) 133–164. <https://doi.org/10.1179/1743280411Y.0000000014>.
- [3] L. Thijs, F. Verhaeghe, T. Craeghs, J. Van Humbeeck, J.P. Kruth, A study of the microstructural evolution during selective laser melting of Ti-6Al-4V, *Acta Mater.* 58 (2010) 3303–3312. <https://doi.org/10.1016/j.actamat.2010.02.004>.
- [4] S. Liu, Y.C. Shin, Additive manufacturing of Ti6Al4V alloy: A review, *Mater. Des.* 164 (2019) 107552. <https://doi.org/10.1016/j.matdes.2018.107552>.
- [5] J.H. Martin, B.D. Yahata, J.M. Hundley, J.A. Mayer, T.A. Schaedler, T.M. Pollock, 3D printing of high-strength aluminium alloys, *Nature.* 549 (2017) 365–369. <https://doi.org/10.1038/nature23894>.
- [6] N.T. Aboulkhair, M. Simonelli, L. Parry, I. Ashcroft, C. Tuck, R. Hague, 3D printing of Aluminium alloys: Additive Manufacturing of Aluminium alloys using selective laser melting, *Prog. Mater. Sci.* 106 (2019). <https://doi.org/10.1016/j.pmatsci.2019.100578>.
- [7] E.O. Olakanmi, R.F. Cochrane, K.W. Dalgarno, A review on selective laser sintering/melting (SLS/SLM) of aluminium alloy powders: Processing, microstructure, and properties, *Prog. Mater. Sci.* 74 (2015) 401–477. <https://doi.org/10.1016/j.pmatsci.2015.03.002>.
- [8] Y.L. Kuo, A. Kamigaichi, K. Kakehi, Characterization of Ni-Based Superalloy Built by Selective Laser Melting and Electron Beam Melting, *Metall. Mater. Trans. A Phys. Metall. Mater. Sci.* 49 (2018) 3831–3837. <https://doi.org/10.1007/s11661-018-4769-y>.
- [9] M. Komarasamy, S. Shukla, S. Williams, K. Kandasamy, S. Kelly, R.S. Mishra, Microstructure, fatigue, and impact toughness properties of additively manufactured nickel alloy 718, *Addit. Manuf.* 28 (2019) 661–675. <https://doi.org/10.1016/j.addma.2019.06.009>.
- [10] S. Gorsse, C. Hutchinson, M. Gouné, R. Banerjee, Additive manufacturing of metals: a brief review of the characteristic microstructures and properties of steels, Ti-6Al-4V and high-entropy alloys, *Sci. Technol. Adv. Mater.* 18 (2017) 584–610. <https://doi.org/10.1080/14686996.2017.1361305>.
- [11] R. Seede, D. Shoukr, B. Zhang, A. Whitt, S. Gibbons, P. Flater, A. Elwany, R. Arroyave, I. Karaman, An ultra-high strength martensitic steel fabricated using selective laser melting additive manufacturing: Densification, microstructure, and mechanical properties, *Acta Mater.* 186 (2020) 199–214. <https://doi.org/10.1016/j.actamat.2019.12.037>.
- [12] P. Agrawal, S. Shukla, S. Thapliyal, P. Agrawal, S.S. Nene, R.S. Mishra, B.A. Mcwilliams, K.C. Cho, Microstructure-property correlation in a laser powder bed fusion processed high strength AF-9628 steel, *Adv. Eng. Mater.* (2020).
- [13] S. Thapliyal, S.S. Nene, P. Agrawal, T. Wang, C. Morphew, R.S. Mishra, B.A. McWilliams, K.C. Cho, Damage-tolerant, corrosion-resistant high entropy alloy with high strength and ductility by laser powder bed fusion additive manufacturing, *Addit. Manuf.* 36 (2020) 101455. <https://doi.org/10.1016/j.addma.2020.101455>.
- [14] P. Agrawal, S. Thapliyal, S.S. Nene, R.S. Mishra, B.A. McWilliams, K.C. Cho, Excellent

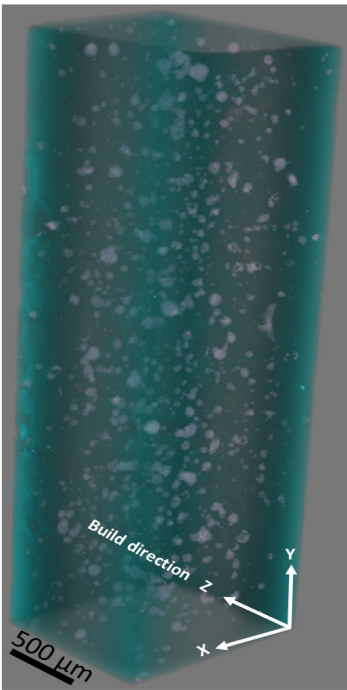
strength-ductility synergy in metastable high entropy alloy by laser powder bed additive manufacturing, *Addit. Manuf.* 32 (2020) 101098. <https://doi.org/10.1016/j.addma.2020.101098>.

- [15] T. DebRoy, H.L. Wei, J.S. Zuback, T. Mukherjee, J.W. Elmer, J.O. Milewski, A.M. Beese, A. Wilson-Heid, A. De, W. Zhang, Additive manufacturing of metallic components – Process, structure and properties, *Prog. Mater. Sci.* 92 (2018) 112–224. <https://doi.org/10.1016/j.pmatsci.2017.10.001>.
- [16] C. Körner, Additive manufacturing of metallic components by selective electron beam melting - A review, *Int. Mater. Rev.* 61 (2016) 361–377. <https://doi.org/10.1080/09506608.2016.1176289>.
- [17] K. Schmidtke, F. Palm, A. Hawkins, C. Emmelmann, Process and mechanical properties: Applicability of a scandium modified Al-alloy for laser additive manufacturing, *Phys. Procedia*. 12 (2011) 369–374. <https://doi.org/10.1016/j.phpro.2011.03.047>.
- [18] N. Read, W. Wang, K. Essa, M.M. Attallah, Selective laser melting of AlSi10Mg alloy: Process optimisation and mechanical properties development, *Mater. Des.* 65 (2015) 417–424. <https://doi.org/10.1016/j.matdes.2014.09.044>.
- [19] S. Thapliyal, M. Komarasamy, S. Shukla, L. Zhou, H. Hyer, S. Park, Y. Sohn, R.S. Mishra, An integrated computational materials engineering-anchored closed-loop method for design of aluminum alloys for additive manufacturing, *Materialia*. 9 (2020). <https://doi.org/10.1016/j.mtla.2019.100574>.
- [20] L. Zhou, H. Hyer, S. Thapliyal, R.S. Mishra, B. McWilliams, K. Cho, Y. Sohn, Process-Dependent Composition, Microstructure, and Printability of Al-Zn-Mg and Al-Zn-Mg-Sc-Zr Alloys Manufactured by Laser Powder Bed Fusion, *Metall. Mater. Trans. A*. (2020) 1–13. <https://doi.org/10.1007/s11661-020-05768-3>.
- [21] S.S. Babu, R. Goodridge, Additive manufacturing, *Mater. Sci. Technol.* (United Kingdom). 31 (2015) 881–883. <https://doi.org/10.1179/0267083615Z.000000000929>.
- [22] I.J. Polmear, *Light Alloys*, Elsevier Ltd, 2005. <https://doi.org/10.1016/B978-0-7506-6371-7.X5000-2>.
- [23] J.R. Davis, *Light Metals and Alloys-Aluminum and Aluminum Alloys*, *Alloy. Underst. Basics.* (2001) 351–416. <https://doi.org/10.1361/autb2001p351>.
- [24] L. Zhou, A. Mehta, E. Schulz, B. McWilliams, K. Cho, Y. Sohn, Microstructure, precipitates and hardness of selectively laser melted AlSi10Mg alloy before and after heat treatment, *Mater. Charact.* 143 (2018) 5–17. <https://doi.org/10.1016/j.matchar.2018.04.022>.
- [25] J. Delahaye, J.T. Tchuindjang, J. Lecomte-Beckers, O. Rigo, A.M. Habraken, A. Mertens, Influence of Si precipitates on fracture mechanisms of AlSi10Mg parts processed by Selective Laser Melting, *Acta Mater.* 175 (2019) 160–170. <https://doi.org/10.1016/j.actamat.2019.06.013>.
- [26] N.T. Aboulkhair, C. Tuck, I. Ashcroft, I. Maskery, N.M. Everitt, On the Precipitation Hardening of Selective Laser Melted AlSi10Mg, *Metall. Mater. Trans. A Phys. Metall. Mater. Sci.* 46 (2015) 3337–3341. <https://doi.org/10.1007/s11661-015-2980-7>.
- [27] D. Koutny, D. Palousek, L. Pantelejev, C. Hoeller, R. Pichler, L. Tesicky, J. Kaiser, Influence of scanning strategies on processing of aluminum alloy EN AW 2618 using selective laser melting, *Materials (Basel)*. 11 (2018). <https://doi.org/10.3390/ma11020298>.
- [28] T. Qi, H. Zhu, H. Zhang, J. Yin, L. Ke, X. Zeng, Selective laser melting of Al7050 powder: Melting mode transition and comparison of the characteristics between the

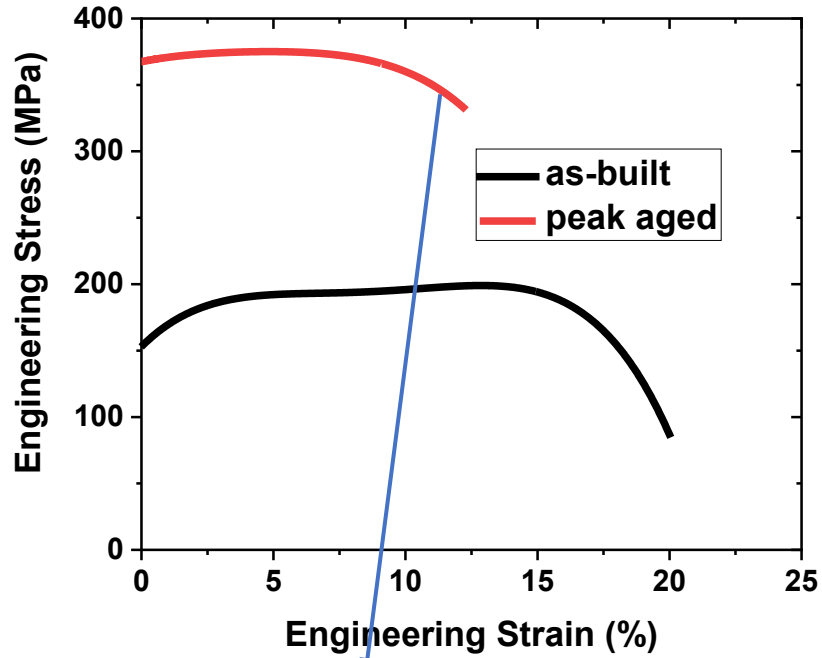
- keyhole and conduction mode, *Mater. Des.* 135 (2017) 257–266. <https://doi.org/10.1016/j.matdes.2017.09.014>.
- [29] N. Kaufmann, M. Imran, T.M. Wischeropp, C. Emmelmann, S. Siddique, F. Walther, Influence of process parameters on the quality of aluminium alloy en AW 7075 using Selective Laser Melting (SLM), in: *Phys. Procedia*, Elsevier B.V., 2016: pp. 918–926. <https://doi.org/10.1016/j.phpro.2016.08.096>.
- [30] P. Wang, C. Gammer, F. Brenne, K.G. Prashanth, R.G. Mendes, M.H. Rümmeli, T. Gemming, J. Eckert, S. Scudino, Microstructure and mechanical properties of a heat-treatable Al-3.5Cu-1.5Mg-1Si alloy produced by selective laser melting, *Mater. Sci. Eng. A* 711 (2018) 562–570. <https://doi.org/10.1016/j.msea.2017.11.063>.
- [31] J. Røyset, N. Ryum, Scandium in aluminium alloys, *Int. Mater. Rev.* 50 (2005) 19–44. <https://doi.org/10.1179/174328005X14311>.
- [32] L.S. Toropova, D.G. Eskin, M.L. Kharakterova, T. V. Dobatkina, Advanced aluminum alloys containing scandium: Structure and properties, Taylor and Francis, 2017. <https://doi.org/10.4324/9781315097541>.
- [33] K.E. Knipling, D.N. Seidman, D.C. Dunand, Ambient- and high-temperature mechanical properties of isochronally aged Al-0.06Sc, Al-0.06Zr and Al-0.06Sc-0.06Zr (at.%) alloys, *Acta Mater.* 59 (2011) 943–954. <https://doi.org/10.1016/j.actamat.2010.10.017>.
- [34] H. Zhang, D. Gu, J. Yang, D. Dai, T. Zhao, C. Hong, A. Gasser, R. Poprawe, Selective laser melting of rare earth element Sc modified aluminum alloy: Thermodynamics of precipitation behavior and its influence on mechanical properties, *Addit. Manuf.* 23 (2018). <https://doi.org/10.1016/j.addma.2018.07.002>.
- [35] N. Qbau, N.D. Nam, N.X. Ca, N.T. Hien, The crack healing effect of scandium in aluminum alloys during laser additive manufacturing, *J. Manuf. Process.* 50 (2020). <https://doi.org/10.1016/j.jmapro.2019.12.050>.
- [36] B.A. Chen, L. Pan, R.H. Wang, G. Liu, P.M. Cheng, L. Xiao, J. Sun, Effect of solution treatment on precipitation behaviors and age hardening response of Al-Cu alloys with Sc addition, *Mater. Sci. Eng. A* 530 (2011) 607–617. <https://doi.org/10.1016/j.msea.2011.10.030>.
- [37] R. Li, M. Wang, T. Yuan, B. Song, C. Chen, K. Zhou, P. Cao, Selective laser melting of a novel Sc and Zr modified Al-6.2 Mg alloy: Processing, microstructure, and properties, *Powder Technol.* 319 (2017) 117–128. <https://doi.org/10.1016/j.powtec.2017.06.050>.
- [38] A.B. Spierings, K. Dawson, T. Heeling, P.J. Uggowitzer, R. Schäublin, F. Palm, K. Wegener, Microstructural features of Sc- and Zr-modified Al-Mg alloys processed by selective laser melting, *Mater. Des.* 115 (2017) 52–63. <https://doi.org/10.1016/j.matdes.2016.11.040>.
- [39] A.B. Spierings, K. Dawson, K. Kern, F. Palm, K. Wegener, SLM-processed Sc- and Zr-modified Al-Mg alloy: Mechanical properties and microstructural effects of heat treatment, *Mater. Sci. Eng. A* 701 (2017). <https://doi.org/10.1016/j.msea.2017.06.089>.
- [40] L. Zhou, H. Hyer, S. Park, H. Pan, Y. Bai, K.P. Rice, Y. Sohn, Microstructure and mechanical properties of Zr-modified aluminum alloy 5083 manufactured by laser powder bed fusion, *Addit. Manuf.* 28 (2019) 485–496. <https://doi.org/10.1016/j.addma.2019.05.027>.
- [41] L. Zhou, H. Pan, H. Hyer, S. Park, Y. Bai, B. McWilliams, K. Cho, Y. Sohn, Microstructure and tensile property of a novel AlZnMgScZr alloy additively manufactured by gas atomization and laser powder bed fusion, *Scr. Mater.* 158 (2019) 24–28.

- https://doi.org/10.1016/j.scriptamat.2018.08.025.
- [42] H. Zhang, H. Zhu, X. Nie, J. Yin, Z. Hu, X. Zeng, Effect of Zirconium addition on crack, microstructure and mechanical behavior of selective laser melted Al-Cu-Mg alloy, *Scr. Mater.* 134 (2017) 6–10. https://doi.org/10.1016/j.scriptamat.2017.02.036.
- [43] X. Nie, H. Zhang, H. Zhu, Z. Hu, L. Ke, X. Zeng, Effect of Zr content on formability, microstructure and mechanical properties of selective laser melted Zr modified Al-4.24Cu-1.97Mg-0.56Mn alloys, *J. Alloys Compd.* 764 (2018) 977–986. https://doi.org/10.1016/j.jallcom.2018.06.032.
- [44] L. Lityńska-Dobrzyńska, Precipitation of phases in Al-Mg-Si-Cu alloy with Sc and Zr additions during heat treatment, in: *Solid State Phenom.*, Trans Tech Publications Ltd, 2007: pp. 163–166. https://doi.org/10.4028/3-908451-40-x.163.
- [45] L.L. Rokhlin, N.R. Bochvar, N.P. Leonova, A. V. Sukhanov, Effect of additional doping with scandium and scandium with zirconium on strength properties of the alloys of Al-Mg₂Si system, *Inorg. Mater.* 52 (2016) 1467–1471. https://doi.org/10.1134/S0020168516150140.
- [46] K. V. Yang, Y. Shi, F. Palm, X. Wu, P. Rometsch, Columnar to equiaxed transition in Al-Mg(-Sc)-Zr alloys produced by selective laser melting, *Scr. Mater.* 145 (2018) 113–117. https://doi.org/10.1016/j.scriptamat.2017.10.021.
- [47] R.S. Haridas, S. Thapliyal, P. Agrawal, R.S. Mishra, Defect-based probabilistic fatigue life estimation model for an additively manufactured aluminum alloy, *Mater. Sci. Eng. A.* (2020) 140082. https://doi.org/10.1016/j.msea.2020.140082.
- [48] Sanya Gupta, P. Agrawal, R.S. Mishra, Corrosion study for marine-based Al-Cu-Sc-Zr alloy fabricated by selective laser melting, (n.d.).
- [49] A. Leicht, C.H. Yu, V. Luzin, U. Klement, E. Hryha, Effect of scan rotation on the microstructure development and mechanical properties of 316L parts produced by laser powder bed fusion, *Mater. Charact.* 163 (2020) 110309. https://doi.org/10.1016/j.matchar.2020.110309.
- [50] S. Kou, *Welding Metallurgy*, John Wiley & Sons, Inc., Hoboken, NJ, USA, 2002. https://doi.org/10.1002/0471434027.
- [51] Y. Kok, X.P. Tan, P. Wang, M.L.S. Nai, N.H. Loh, E. Liu, S.B. Tor, Anisotropy and heterogeneity of microstructure and mechanical properties in metal additive manufacturing: A critical review, *Mater. Des.* 139 (2018) 565–586. https://doi.org/10.1016/j.matdes.2017.11.021.
- [52] Z. Wang, T.A. Palmer, A.M. Beese, Effect of processing parameters on microstructure and tensile properties of austenitic stainless steel 304L made by directed energy deposition additive manufacturing, *Acta Mater.* 110 (2016) 226–235. https://doi.org/10.1016/j.actamat.2016.03.019.
- [53] E.A. Marquis, D.N. Seidman, Nanoscale structural evolution of Al₃Sc precipitates in Al(Sc) alloys, *Acta Mater.* 49 (2001) 1909–1919. https://doi.org/10.1016/S1359-6454(01)00116-1.
- [54] G. Wang, H. Ouyang, C. Fan, Q. Guo, Z. Li, W. Yan, Z. Li, The origin of high-density dislocations in additively manufactured metals, *Mater. Res. Lett.* 8 (2020) 283–290. https://doi.org/10.1080/21663831.2020.1751739.
- [55] J.H. Robinson, I.R.T. Ashton, E. Jones, P. Fox, C. Sutcliffe, The effect of hatch angle rotation on parts manufactured using selective laser melting, *Rapid Prototyp. J.* 25 (2019) 289–298. https://doi.org/10.1108/RPJ-06-2017-0111.

Additively manufactured Al-Cu-Sc-Zr alloy



good
printability



Cu-rich and $\text{Al}_3\text{Sc}/\text{Al}_3(\text{Sc},\text{Zr})$ precipitates
improving the strength

